https://doi.org/10.1631/bdm.2400276
Received: 14 July 2024 / Accepted: 19 October 2024

RESEARCH ARTICLE

A dual-functional capsule robot for drug delivery and tissue biopsy based on magnetic torsion spring technology

Preprint of Bio-Design and Manufacturing (submitted)

Qing Cao1,2, Yue Pan1,2, Yangqianhui Zhang1,2, Yuning Jiang1,2, Guofang Gong1,2, Huayong Yang1,2, Fuzhou Niu3✉, Dong Han1,2✉

1 State Key Laboratory of Fluid Power and Mechatronic Systems, Zhejiang University, Hangzhou 310058, China
2 School of Mechanical Engineering, Zhejiang University, Hang-zhou 310058, China
3 School of Mechanical Engineering, Suzhou University of Sci-ence and Technology 215009, China

✉ Fuzhou Niu fzniu@usts.edu.cn
✉ Dong Han dong_han@zju.edu.cn

Abstract

Wireless capsule endoscopy (WCE) has the potential to fully replace conventional wired counterparts for its low aggression. Recent studies have attempted to expand the functions of capsules toward this goal. However, limitations in space and energy supply have resulted in the inability to perform multiple diagnostic and treatment tasks using a single capsule. In this study, we developed a dual-function capsule robot (DFCR) for drug delivery and tissue biopsy based on magnetic torsion spring technology. The delivery module was shown to rotate the push rod with a thrust of 894 mN to release approximately 0.3 mL of semisolid drug. The biopsy module used a built-in blade to cut tissue with a shear stress of 22.87 MPa, producing a sample of approximately 1.8 mm^3. Additionally, a five-degree-of-freedom permanent magnet drive system was developed. By adjusting the strength of the unidirectional magnetic field generated by an external magnet, the capsule can be wirelessly controlled to sequentially trigger the two functions. Ex vivo

tests on porcine stomachs confirmed the feasibility of the prototype capsule ($\phi 12 \times 45$ mm) in active movement, medication, and tissue biopsy. The newly developed DFCR further expands the clinical application prospects of WCE robots in minimally invasive surgery.

Graphic abstract

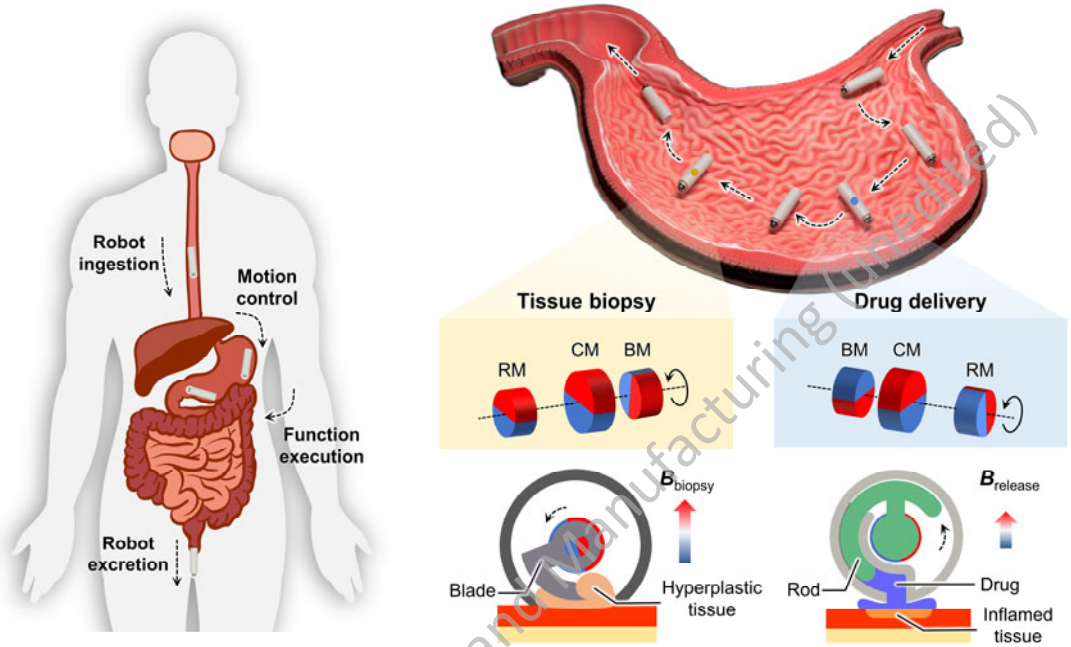

Preprint of Bio-Design and Manufacturing (Unedited)

Keywords: Wireless capsule endoscopy (WCE) · Dual-function capsule robot (DFCR) · Magnetic torsion spring (MTS) · Drug delivery · Tissue biopsy · Permanent magnet

1 Introduction

Insufficient attention to dietary health has led to an increasing incidence of gastric diseases annually [1]. If left untreated, symptoms such as inflammation, ulcers, and bleeding can progress to a potentially cancerous state [2,3]. Currently, electronic endoscopy is considered the gold standard for diagnosing and treating gastrointestinal diseases [4]. It involves inserting a long cable into the patient's body cavity, enabling clear observation of the target tissue and offering viable treatment options [5]. However, these traditional procedures often cause significant discomfort and are associated with risks such as infection and perforation, which makes them intolerable for some patients [6, 7]. The advent of wireless capsule endoscopy (WCE) has effectively circumvented these issues.

Since the launch of the first commercial capsule endoscope M2A by Given Imaging, Ltd (Israel). in 2001 [8], various advancements have been achieved in WCE. One notable example is the integration of a circular magnet into the capsule endoscope, which has transformed the movement of capsules from passive to active, offering a more comprehensive view of the stomach and intestines (NaviCam^{TM} from Ankon Co., Ltd, China.) [9]. Despite the enhancements in mobility and imaging, significant incentives for

the widespread adoption of these capsules are still lacking. To fully replace traditional wired endoscopy, substantial improvements in the diagnostic and therapeutic capabilities of WCE are necessary.

Recent studies have focused on developing capsule robots with diagnostic and therapeutic capabilities based on commercial WCE devices. These robots are equipped with tools like biopsy needles, scrapers, and micro forceps for submucosal tissue biopsy sampling [10], or compartments and patches for drug storage and release [11, 12]. Different power sources have been explored for expanding capsule functionality, including thermoelectric effects [13], micro motors [14, 15], shape memory alloys [16], and magnetic fields [17-21]. However, the first three options may prematurely drain the energy of the original button batteries before the completion of a full gastrointestinal examination [22]. The incorporation of numerous complex mechanical components into the capsules also hinders these from being compact. Magnetic driving is considered an optimal scheme due to its contactless operation and high reliability, which eliminate the need for an additional electrical power supply, thus attracting significant interest [23]. For example, based on the soft Sarrus linkage concept, Sitti et al. [17] designed a capsule capable of moving back and forth in an external magnetic field to perform multiple biopsies. Ye et al. [24] utilized the same-direction repulsion principle of two circular permanent magnets in an external magnetic field to extend the biopsy forceps from the capsule for sampling. It is crucial to note that, whether involving a single magnet reciprocating or the attraction-repulsion switching mechanism of the magnets, these axial magnet arrangement strategies will occupy significant space, limiting the ability of a single capsule to perform multiple diagnostic and therapeutic tasks.

The magnetic torsion spring (MTS) is a novel magnetic mechanical elastic element that can be remotely loaded by altering the surrounding magnetic field and can also store and release mechanical energy upon external activation. This concept was first introduced by Simi et al. [25], who incorporated two radial magnets and a scraper within the capsule to sample tissues using the torque generated by the instantaneous switching of the magnetic moment direction from parallel to opposite. Subsequently, Zhou et al. [26] modified the end effector of the MTS to a mechanical structure that could increase the capsule's diameter, enabling the remote anchoring of the capsule endoscope. Characterized by its unique radial arrangement, the MTS offers advantages in integration and energy release, making it suitable for multifunctional expansion of the capsule.

In this study, we developed a highly integrated dual-functional capsule robot (DFCR) incorporating an improved MTS mechanism. The innovative MTS module, equipped with three magnets, can react to external magnetic fields to produce two working torques, thereby activating the drug delivery and tissue biopsy functions of the DFCR in sequence. Additionally, a five-degree-of-freedom permanent magnet drive system was designed to generate the required magnetic field for controlling the DFCR's actions. Ex vivo experiments on porcine stomachs confirmed the feasibility of the prototype capsule in executing these functions.

Preprint of Biomedical and Manufacturing Engineering

2 Robot structure design

2.1 Capsule overview

Figure 1a illustrates a specific scenario in which the DFCR is applied in the stomach, where it performs both the functions of drug delivery and biopsy sampling. The patient swallows the DFCR with water, allowing it to move from the esophagus to the stomach through peristalsis. By applying a low-intensity external magnetic field, $\boldsymbol{B}_{\text{turn}}$, the operator can adjust the capsule's orientation to bring the suspected lesion within sight. The capsule's movement to the first target location is facilitated by alternating $\boldsymbol{B}_{\text{turn}}$ with a rolling magnetic field, $\boldsymbol{B}_{\text{roll}}$. Upon detecting inflammation in the tissue, the MTS is activated via a medium-intensity unidirectional magnetic field, $\boldsymbol{B}_{\text{release}}$, to release the stored drug. Subsequently, the DFCR is redirected and piloted to the second target site, which contains hyperplastic tissue, using the same low-intensity external magnetic field. A high-intensity unidirectional magnetic field, $\boldsymbol{B}_{\text{biopsy}}$, then reactivates the MTS to capture the tissue sample that enters the capsule through the notch with a blade. The procedure ends with the robotic capsule exiting the stomach and eventually being excreted for the pathological evaluation of samples.

The DFCR consists of four modules: a camera module, an MTS module, a drug delivery module, and a tissue biopsy module (Fig. 1b). The camera module, situated at the front of the capsule, is modeled after a commercial capsule endoscope that is mainly used for observing potentially abnormal tissue. Since its design is well-documented, further details will not be discussed in this section.

Preprint of Bio-Design and Manufacturing (unedited)

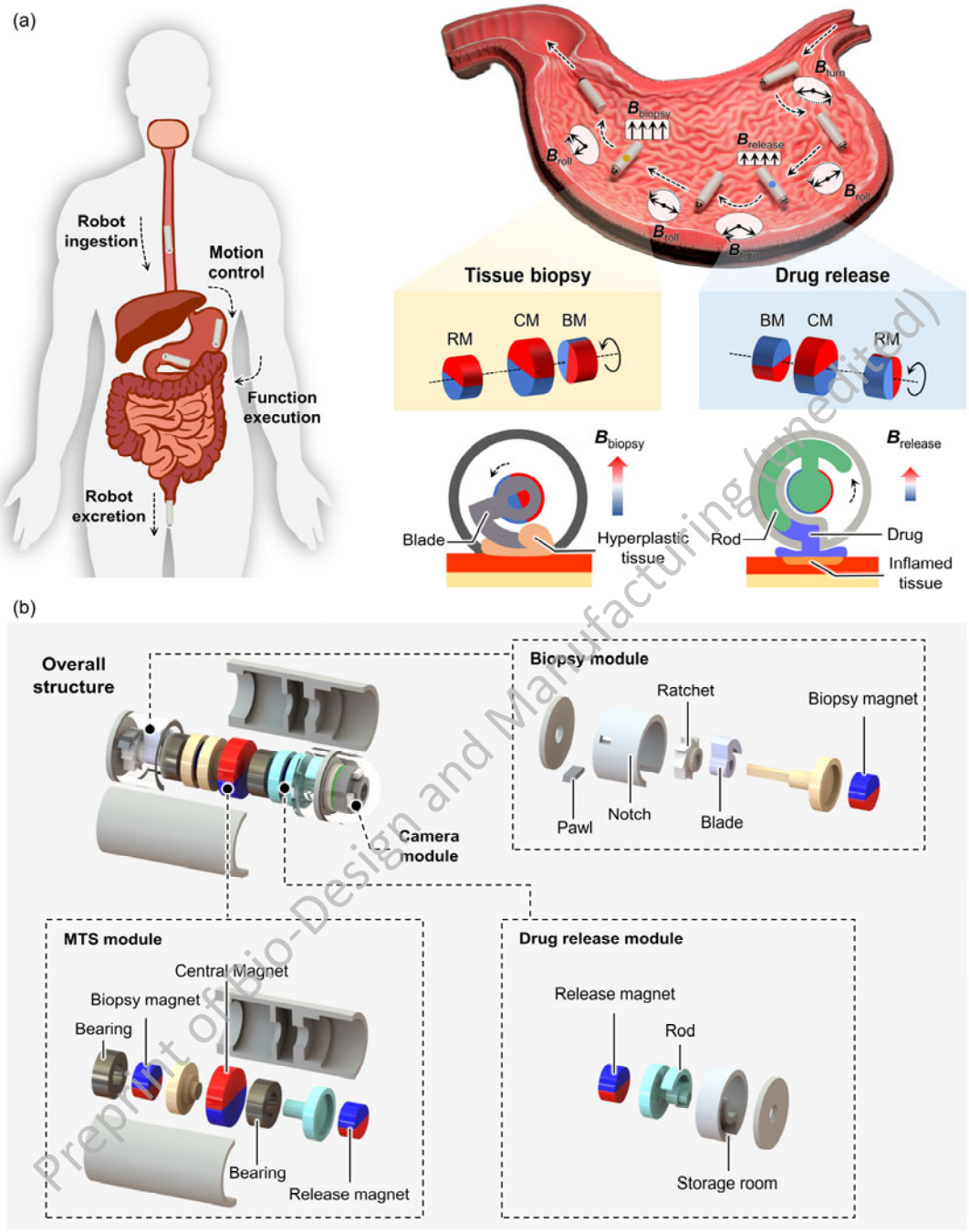

Preprint of Bio-Design and Manufacturing (Unedited)

Figure 1 Conceptual design of the proposed DFCR. (a) Specific scenario in which the DFCR is applied in the stomach. The procedure involves the capsule entering the stomach propelled by the peristaltic force of the digestive tract and performing surgical functions while being controlled by an external magnetic field. (b) Robotic overall structure and detailed design. Abbreviations: RM, release magnet; CM, central magnet; BM, biopsy magnet; MTS, magnetic torsion spring.

2.2 MTS module

The MTS module, located in the middle of the capsule, serves a dual purpose: driving the robot to the target area and supplying the necessary working torques for drug release and tissue biopsy. It mainly comprises a central magnet (CM), release magnet (RM), and biopsy magnet (BM), all of which are cylindrical magnets radially magnetized and aligned along the capsule's axis. While they share the same thickness, the CM has a larger diameter. The BM is positioned closer to the CM along the axis than the RM. The CM remains stationary within the capsule, whereas the RM and BM are placed on either side of it, which allows them to rotate freely but not move along the robot's axis. Upon activation by an external magnetic field, the RM and BM rotate, delivering the torques to the corresponding module for the execution of minimally invasive surgery.

Figure 2 depicts the working principle of the MTS. Initially, no external magnetic field or a weak magnetic field is present, and the magnetic moments of the three magnets are parallelly aligned (Fig. 2a). During this phase, the rotational movements of the RM and BM are constrained by the magnetic coupling torque so that their initial positions are maintained, as shown by the rotation angles θ_1 and θ_2 of the two magnets relative to CM being both 0. As the external magnetic field increases along the direction of the CM's magnetic moment, the torques applied to the RM and BM also increase. Due to the greater axial distance (d_1) between the RM and CM compared with the distance (d_2) between the BM and CM, the magnetic torque exerted by the CM on the RM is lower than that on the BM. As a result, the RM reaches the torque threshold of the CM before the BM, and the mechanical energy released from the MTS under the influence of the external magnetic field causes its rotation ($\theta_1 = \pi$). Meanwhile, the BM remains in its original state ($\theta_2 = 0$) as it has not yet surpassed the torque from the CM (Fig. 2b). Subsequently, as the external magnetic field further strengthens, the BM eventually overcomes the combined torque from the CM and RM, which leads to its alignment with the CM's magnetic orientation ($\theta_2 = \pi$) (Fig. 2c). Finally, as the external magnetic field weakens, both the BM and CM return to their initial positions sequentially.

The improved MTS primarily involves a fusion of two basic MTSs (MTS_r and MTS_b). MTS_r, containing the CM and RM, is utilized for drug delivery, while MTS_b, comprising the CM and BM, is employed for lesion biopsy.

Preprint of Bio-design and Manufacturing (unedited)

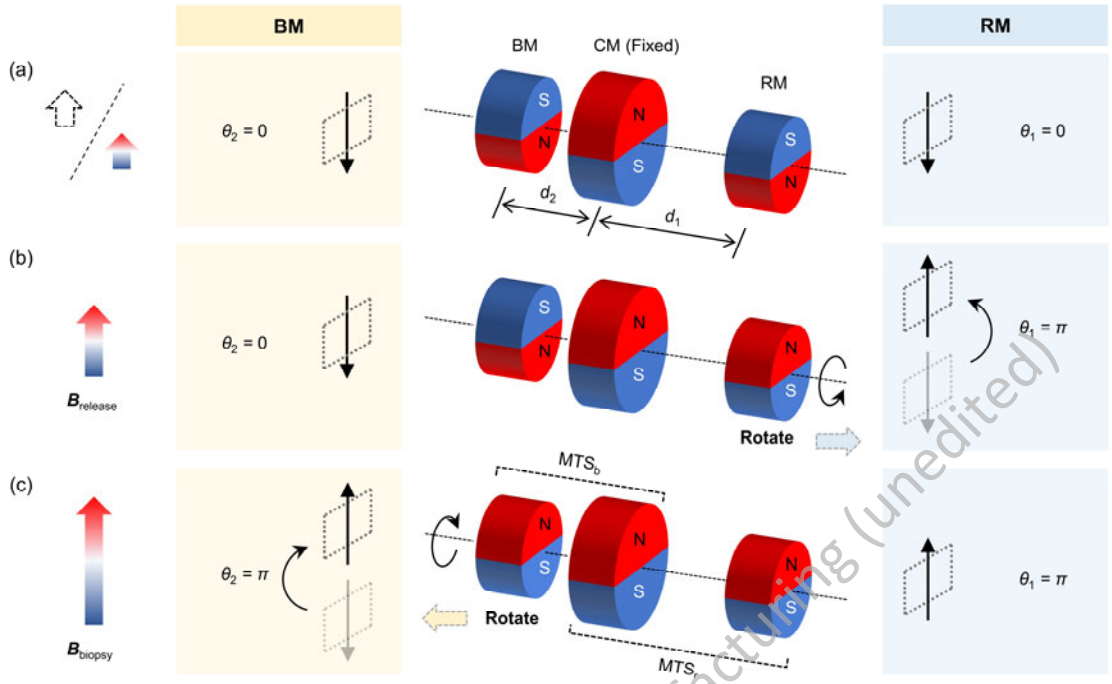

Figure 2 Working mechanism of the MTS. (a)-(c) represent the states of the BM and RM under different external magnetic field strengths. (a) No external magnetic field or low-intensity external magnetic field. (b) Medium-intensity unidirectional magnetic field. (c) High-intensity unidirectional magnetic field.

Preprint of Bio-Design and Manufacturing (unedited)

2.3 Drug delivery module

Figure 3a shows in detail the process of drug release from the drug delivery module positioned between the camera and the MTS modules. Initially, the semisolid drug remains stored in the chamber until the capsule reaches the target area, as there is no magnetic field strong enough to activate the rotation action of the RM. When the outlet aligns with the inflamed region, a stronger external magnetic field is applied to engage the MTS_r. This causes the RM to turn and transfer torque to the axially connected rod, pushing the drug out toward the target site. Explanations in Section 2.2 have indicated that the BM remains nearly stationary, thus segregating the biopsy procedure. Once all drugs are dispensed from the storage chamber, the external magnetic field is removed. The RM and the rod return to their original positions under the influence of the magnetic coupling torque.

The volume of the drug released by the rotation of the rod is expressed as follows:

$$V_{\text{drug}} = \frac{1}{2}\beta\left(R_{\text{out}}^2 - R_{\text{in}}^2\right)d, \quad (1)$$

where β represents the rotation angle of the rod, R_{out} and R_{in} are the outer and inner radii of the rod, respectively, and d is the chamber depth. In general, the release volume of 0.3 mL of targeted drug is sufficient to meet the medical treatment criteria [27], from which the size of R_{out}, R_{in}, and d can be determined.

In this study, it was essential to evaluate the force required to expel 0.3 mL of medication from the storage chamber to the target tissue. The outlet was modeled as a straight circular needle, with a length of 1 mm and an inner diameter of 1.4 mm. The Poiseuille equation was employed to simulate the flow of medication through the needle [28]. The flow rate was calculated as follows:

$$Q_f = \frac{\pi r^4 (P_2 - P_1)}{8 n_v l}, \quad (2)$$

where r is the radius of the needle's bore, n_v is the viscosity of the medication, and l is the length of the needle. P_1 represents the pressure at the end of the needle, which is 0 because the drug was released onto the tissue surface, while P_2 is the pressure required to expel the medication. For n_v, the semisolid medication [consisting of polyvinyl alcohol (PVA 1795) gel] typically behaves as a plastic fluid, with its viscosity decreasing as the shear rate increases. To approximate the Poiseuille equation, which assumes an ideal Newtonian fluid, it was necessary to determine the effective viscosity of the medication. Here, it was measured at 5.8 $\mathrm{Pa} \cdot$ s using a viscometer at room temperature, under a conventional shear rate of 1 s^{-1} at a concentration of 10%, which ensured the effective expulsion of the semisolid medication. The administration time was set to 1 s, and the flow rate Q_f was calculated by dividing the volume of medication stored in the delivery module by the target delivery time. By rearranging the equation, it was possible to determine the pressure P_2 required for medication delivery; this value was subsequently multiplied by the cross-sectional area of the plunger in the chamber to obtain the delivery force $\boldsymbol{F}_r$ necessary to expel the medication, which was estimated to be approximately 554 mN.

Preprint of Bio-Design and Manufacturing (in editing)

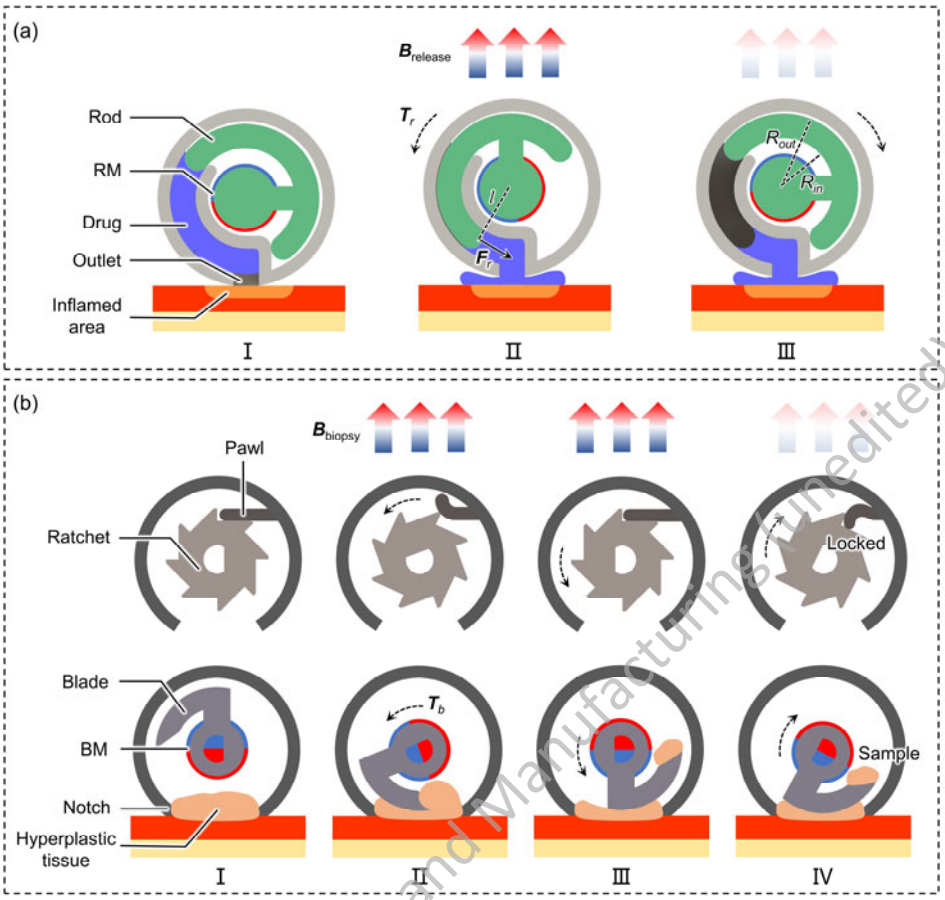

Figure 3 Detailed illustrations of the two modules for (a) drug delivery and (b) tissue biopsy.

Preprint of Bio-Design and Manufacturing (unedited)

2.4 Tissue biopsy module

The biopsy module of the DFCR's end utilizes a rotating blade for sampling, as shown in Fig. 3b. Along with a rigid ratchet, this blade is connected to the shaft embedded with the BM. A one-way rotational mechanical structure was established through the interaction between a flexible pawl inside the capsule shell and the rigid ratchet.

The biopsy procedure consisted of four stages. Initially, the capsule was positioned in the lesion to allow the target hyperplastic tissue to enter the robot through the notch. Next, a high-intensity external magnetic field was applied to activate the MTS_b for tissue biopsy. The BM rotated counterclockwise, propelling the blade to collect suspicious tissues. Simultaneously, the rigid ratchet moved in the same direction as the BM without being constrained by the pawl. Once the sampling was completed, the external magnetic field was turned off. The magnetic coupling with the CM caused the BM, ratchet, and blade to attempt to return to their original positions due to the torque effect. However, the clockwise rotation of the ratchet was impeded by the elastic pawl, effectively locking the BM. This ensured that the harvested tissue remained securely stored within the capsule, preventing any potential contamination or leakage. Despite the RM's rotation induced by the magnetic field, the sampling process was not affected, as the drug had already been delivered, ensuring that no drug residues were left in the capsule.

The total rotation angle of the blade is π during the biopsy procedure. The shear stress $\boldsymbol{\tau}_b$ capable of executing biopsy sampling from the tissue of interest is expressed by the following equation:

$$\boldsymbol{\tau}_b = \frac{\boldsymbol{T}_b}{k \cdot t \cdot s}, (3)$$

where $\boldsymbol{T}_b$ is the rotational torque generated by the BM, and $k, t,$ and s are the working radius, thickness, and width of the blade, respectively. To ensure effective lesion sampling, it is recommended to maintain $\boldsymbol{\tau}_b$ at least 20 Mpa [20].

The sample amount obtained by scraping using the blade was calculated as

$$V_{\text{sample}} = t \cdot s \cdot h, (4)$$

where h is the thickness of the collected tissue. The amount of sampled tissue should range from 1 to 5 mm^3 to ensure the feasibility of subsequent histological analyses [29, 30].

3 Analytical model of magnetic fields

To effectively perform minimally invasive surgery using the DFCR, it was crucial to conduct a preliminary evaluation of its functional response and motion control via simulation. This evaluation was necessary to determine whether the triggering magnetic field strength of the MTS and its corresponding operating torque met the desired requirements.

3.1 Functional simulation model

It was first essential to accurately set the dimensions and positions of the three magnets in the MTS. The CM should have a larger diameter than the BM and RM on both sides due to its dominant role in exerting the magnetic coupling torque. Given that drug delivery occurs before tissue biopsy, the torque exerted by the CM on the RM should be weaker than that on the BM, indicating a longer axial distance between the former two magnets. Moreover, to develop a highly integrated capsule robot prototype suitable for clinical applications, the magnet sizes should be minimized under an excitation magnetic field.

A finite element simulation analysis of the MTS was conducted using ANSYS Maxwell software. The external magnetic field was generated by an external permanent magnet (EPM) measuring 40 mm in diameter and 30 mm in thickness. The CM had a diameter of 10 mm and a thickness of 3 mm, while the RM and BM had a diameter of 6 mm and same thickness as the CM. The axial distance between the RM and the CM was 7 mm, while that between the BM and the CM was only 2 mm. All the magnets had a magnetization strength of 890,000 A/m(N35).

Based on the magnetic dipole theory, the magnetic field $\boldsymbol{B}(\boldsymbol{p})$ at point $\boldsymbol{p}$ generated from a permanent magnet is expressed by the following equation:

$$\boldsymbol{B}(\boldsymbol{p}) = \frac{\mu_0 |\boldsymbol{m}|}{4\pi |\boldsymbol{r}|^3} \left(3\hat{\boldsymbol{r}}\hat{\boldsymbol{r}}^{\mathrm{T}} - I\right)\hat{\boldsymbol{m}}, (5)$$

Preprint of 3D Design and Manufacturing (Unedited)

where μ_0 is vacuum magnetic permeability and the value is $4\pi \times 10^{-7}\mathrm{Tm} \cdot \mathrm{A}^{-1}$, I is the 3×3 identity matrix, $\boldsymbol{m}$ is magnetic dipole moment, $\boldsymbol{r}$ is the vector from the center of the EPM to position $\boldsymbol{p}$, and $\hat{\boldsymbol{r}}$ and $\hat{\boldsymbol{m}}$ are the unit vectors of $\boldsymbol{r}$ and $\boldsymbol{m}$, respectively.

When there is no external magnetic field ($\boldsymbol{B}_{\mathrm{out}}$) present, the torques applied from the CM on the RM and BM are represented as $\boldsymbol{T}_{\mathrm{in}}$($\boldsymbol{T}_{\mathrm{inr}}$ and $\boldsymbol{T}_{\mathrm{inb}}$). The torques exerted by the EPM on the RM and BM are denoted as $\boldsymbol{T}_{\mathrm{out}}$($\boldsymbol{T}_{\mathrm{outr}}$ and $\boldsymbol{T}_{\mathrm{outb}}$). Since the magnetization direction of the EPM aligned with that of the CM, no torque would be exerted on the CM. These two torques were calculated as

$$\boldsymbol{T}_{\mathrm{in}} = \boldsymbol{T}_{\mathrm{peak}} \sin(\alpha - \alpha'), (6)$$

$$\boldsymbol{T}_{\mathrm{out}} = \boldsymbol{m}_{\mathrm{load}} \times \boldsymbol{B}_{\mathrm{out}}, (7)$$

where $\boldsymbol{T}_{\mathrm{peak}}$ represents the peak torque; α and α' represent the rotation angles of the load-side (BM or RM) and drive-side (CM) in each basic MTS, respectively; the difference $\alpha - \alpha'$ denotes the relative angular displacement; and $\boldsymbol{m}_{\mathrm{load}}$ is the magnetic moment for the loaded magnet. Due to the alignment of the external magnetic field that activated the MTS with the CM, the rotation angle of the CM remained at zero ($\alpha' = 0$).

According to the simulation analysis of the basic MTS (Fig. 4a), $\boldsymbol{T}_{\mathrm{in}}$ reached its maximum value when $|\alpha| = \pi/2$. In the presence of the activated magnetic field environment created by the EPM, the total torque acting on the BM was a combination of $\boldsymbol{T}_{\mathrm{in}}$ and $\boldsymbol{T}_{\mathrm{out}}$. As the external magnetic field intensified (Fig. 4b), the total torque changed its direction, indicating that the torque exerted by the EPM on the RM exceeded that applied by the CM. During this time, the RM rotated as its magnetic moment gradually aligned with the external magnetic field, producing torque. When the direction of this magnetic moment became perpendicular to the CM's magnetic moment direction, the torque reached its peak value.

To comprehensively analyze the improved MTS, a finite element simulation of the four magnets was also conducted (Fig. 4c). The magnetic moment direction of the EPM was aligned with the CM and positioned at a vertical distance of 69 mm from the MTS. Figure 4d displays the distribution of the simulated magnetic field strength produced by the EPM. In this configuration, the RM and BM remained in their initial positions without rotating. Another simulation was performed wherein the EPM-MTS distance was gradually adjusting from 80 mm to 30 mm with a step size of 1 mm. The torque comparisons shown in Fig. 4 e indicate that the RM and BM began rotating at distances of 61 mm and 43 mm from the EPM, which corresponded to magnetic field strengths of 18.2 mT and 71.3 mT, respectively.

The working torques of the RM and BM had to exceed the minimum required values to ensure effective drug delivery and tissue biopsy. When the distance between the EPM and MTS was 44 mm during drug delivery, the external magnetic field strength reached 65.3 mT. At this point, the RM rotated with a torque of 3.10 mNm, while the BM remained stationary. In the case of a rotation radius of 3.5 mm, the drug thrust $\boldsymbol{F}_r$ was determined to be 886 mN, which exceeded the necessary 554 mN. For tissue sampling, the distance was reduced to 34 mm, and the magnetic field strength increased to 154.4 mT, resulting in a torque of 6.85 mNm on the BM. The blade dimensions were 0.03 mm in thickness and 2 mm in width. By applying Eq. (3) with a working radius of 5 mm, the resulting shear stress $\boldsymbol{\tau}_b$ was calculated to be 22.83 MPa, meeting the required standards.

Preprint of Bio-Design and Manufacturing (unedited)

In addition to torque estimation, it was equally important to analyze the anchoring force of the capsule to ensure the stability of the surgical procedure. The non-uniform strength of the external magnetic field generated by the EPM not only enabled the active motion and functional triggering of the DFCR but also provided the necessary anchoring force. This anchoring force is determined by the attractive and repulsive forces between the MTS and EPM. Gastric peristalsis can interfere with the capsule's position, potentially displacing the robot from the target area. Therefore, a stronger anchoring force can help reduce these adverse effects.

The anchoring force $\boldsymbol{F}_a$ exerted by the EPM on the magnets inside the capsule is described as

$$\boldsymbol{F}_a = (\boldsymbol{m}_c \cdot \nabla)\boldsymbol{B}_{\text{out}}, \quad (8)$$

where $\boldsymbol{m}_c$ represents the magnetic moment of the magnet inside the capsule, and ∇ is the gradient operator. The obtained force values are reported in Fig. 4f, indicating the presence of three stages: the initial unactivated MTS (Phase I), the triggered MTS_r (Phase II) for drug release, and the activated MTS_b for biopsy (Phase III). As the strength of the external magnetic field increased, the RM and BM gradually aligned with the direction of the external magnetic field, increasing the attractive force on the capsule and reducing the repulsive force. This led to an upward trend in the anchoring force, especially in Phase III, ensuring the capsule's resistance to interference.

Preprint of Bio-Design and Manufacturing (Unedited)

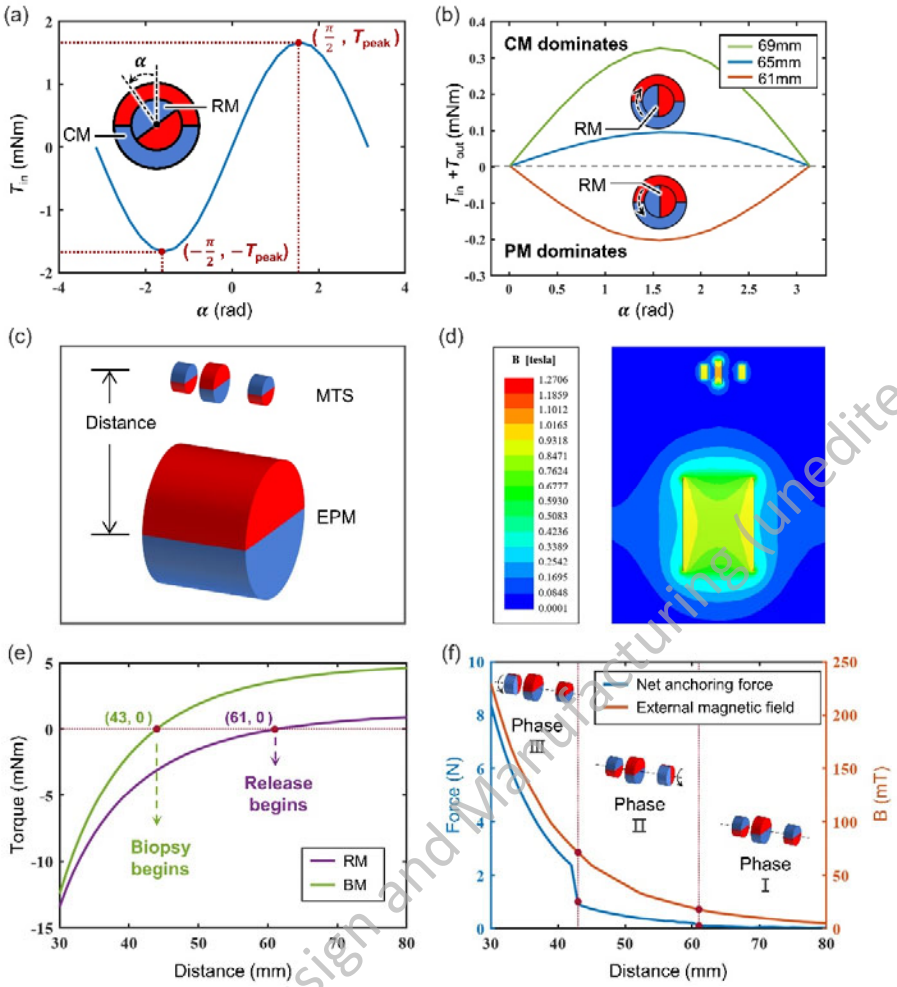

Figure 4 Simulation analysis. (a) Variation of the torque exerted by the CM on the RM with angle α. (b) Tendency for alteration of the vector sum of $\boldsymbol{T}_{\text{in}}$ and $\boldsymbol{T}_{\text{out}}$ acting on the RM as the EPM approaches. (c) Model of the MTS and EPM. (d) Magnetic field distribution at a vertical distance of 69 mm between the EPM and MTS. (e) Comparison of the release and biopsy torques as the EPM approaches. (f) Analysis of the anchoring force. Abbreviations: EPM, external permanent magnet.

Preprint of Bio-Design and Manufacturing (unedited)

3.2 Active motion control model

Accurate control of the capsule robot motion facilitates precise examination of specific areas within the gastrointestinal tract, thereby improving diagnostic and therapeutic capabilities. Currently, the magnetic fields used for driving these robots are generated either through electromagnetic coils [31] or a permanent magnet [32]. Electromagnetic coils produce uniform and gradient magnetic fields by strategically arranging and controlling the current [33,34]. Conversely, the permanent magnet, acting as the end effector of the robotic arm, generates the required magnetic field directly by adjusting its position and orientation. Simulation results of magnetic fields in Section 3.1 show that a

permanent magnet can effectively initiate the active motion and functions of the DFCR. Due to its strong magnetic field, low installation cost, and simple operation, we opted to analyze the capsule motion control via permanent magnet driving (PMD).

Two distinct motion control modes were established (Fig. 5). The first was a destination-reaching mode to drive the capsule toward the target location; the second was an orientation-adjusting mode to align the surgical device within the capsule with the lesion. Throughout the active motion process, the three magnets that constituted the MTS remained fixed relative to the capsule body. For the sake of simplifying the analysis, these magnets were treated as a single entity, and the forces and torques acting on them were calculated via vector composition.

In the destination-reaching mode, the EPM executed simultaneous horizontal movements and rotations to generate a composite magnetic field comprising rotating and gradient components. The DFCR navigated to the target area via a combination of sliding and rolling motions. The sliding motion was driven by the gradient magnetic field, while the rolling motion was induced by the rotating magnetic field. The capsule's sliding motion was calculated as follows:

$$\omega \frac{d^2 \boldsymbol{x}_c}{dt^2} = \boldsymbol{F}_{\text{sum},h} - \text{sgn}\left(\frac{d\boldsymbol{x}_c}{dt} - \frac{d\boldsymbol{\theta}_c}{dt} e\right) \mu_f \left(\boldsymbol{F}_{\text{sum},v} + \omega \boldsymbol{g}\right), \quad (9)$$

where ω and e denote the mass and radius of the capsule, respectively, while $\boldsymbol{x}_c$ and $\boldsymbol{\theta}_c$ represent the horizontal displacement and rotational angle of the DFCR around its axis, respectively. $\boldsymbol{F}_{\text{sum},h}$ and $\boldsymbol{F}_{\text{sum},v}$ refer to the total magnetic force vectors in the horizontal and vertical directions, respectively, resulting from the interactions between the MTS and the EPM. With regard to the frictional force, the normal support force is the vector sum of $\boldsymbol{F}_{\text{sum},v}$ and the gravitational force of the capsule ($\omega \boldsymbol{g}$), with the friction coefficient between the capsule and the gastrointestinal tract denoted as μ_f. The direction of the frictional force depends on the relative velocity between the rotational and transversal velocities, and a sgn function is suitable to represent this characteristic. If the rotational speed exceeds the translational speed, rotation dominates, propelling the capsule forward due to friction; otherwise, friction hinders movement in the opposite direction. During rotational motion, the capsule rotated around its axis ($\boldsymbol{n}_{ad}$), as described by the following motion equation:

$$I_{ad} \frac{d^2 \boldsymbol{\theta}_c}{dt^2} = \boldsymbol{\tau}_{\text{sum},ad} - \left[\text{sgn}\left(\frac{d\boldsymbol{x}_c}{dt} - \frac{d\boldsymbol{\theta}_c}{dt} e\right) \mu_f \left(\boldsymbol{F}_{\text{sum},v} + \omega \boldsymbol{g}\right)\right] e, \quad (10)$$

where I_{ad}, $\boldsymbol{\tau}_{\text{sum},ad}$ are moment inertial for the capsule and the sum of magnetic torque along axis $\boldsymbol{n}_{ad}$, respectively.

In the orientation-adjusting mode, the DFCR rotated around the radial axis $\boldsymbol{n}_{rd}$ to bring the diseased area in the field of view. The devices performing minimal surgery, including the blade and drug-pushing rod, were positioned directly at the target tissue. There was no rolling motion involved in the entire adjusting process, so the direction of the friction force remained opposite to that of the rotation. The following motion equation was obtained:

$$I_{rd} \frac{d^2 \boldsymbol{\varphi}_c}{dt^2} = \boldsymbol{\tau}_{\text{sum},rd} - \int_0^H \mu_f \left(\boldsymbol{F}_{\text{sum},v} + \omega \boldsymbol{g}\right) dh, \quad (11)$$

Preprint of Bio-Design and Manufacturing (Unedited)

where I_{rd} represents the moment of inertia, which is not equal to $\boldsymbol{I}_{ad}$ due to the different rotation radii; H is the length of the capsule; and $\boldsymbol{\tau}_{\text{sum},rd}$ and $\boldsymbol{\varphi}_c$ are the sum of the magnetic torque and rotation angle around the radial axis $\boldsymbol{n}_{rd}$, respectively.

The surgical procedure executed by the DFCR involved switching between the two modes of movement. Initially, the capsule used the front camera to locate the lesion while in the orientation-adjusting mode. It then switched to the destination-reaching mode, guided by a mixed magnetic field, to reach the desired site. Subsequently, the capsule adjusted the outlet of the drug release module toward the lesion in the orientation-adjusting mode. When the unidirectional magnetic field activated the basic MTS for drug delivery, the stored drug was released into the target area. This process was repeated to guide the capsule to the target location, where tissue biopsy was performed using a stronger unidirectional magnetic field, allowing the sample to be removed by the blade inside the capsule. Once all surgical tasks were completed, the capsule was driven away from the stomach.

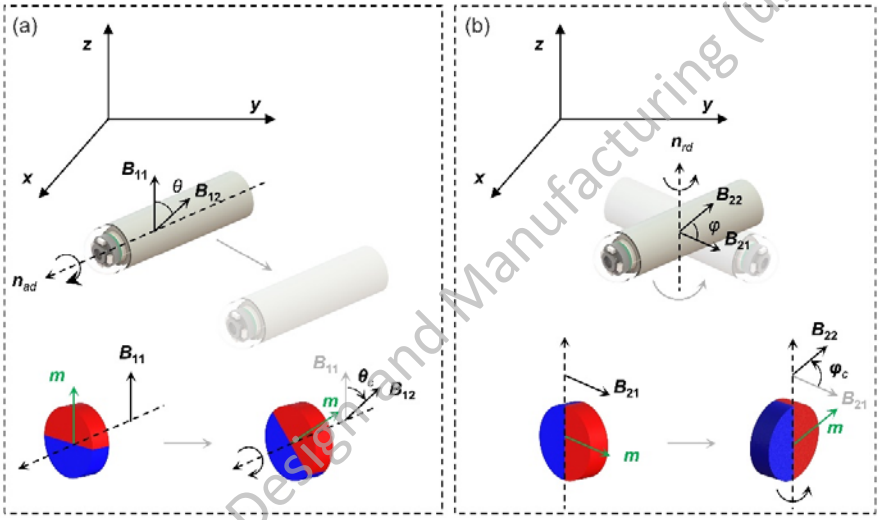

Figure 5 Model of the capsule's active motion control. (a) Destination-reaching mode. (b) Orientation-adjusting mode. $\boldsymbol{B}_{11}$, $\boldsymbol{B}_{12}$, $\boldsymbol{B}_{21}$, and $\boldsymbol{B}_{22}$ represent the directions of the external magnetic field at different times.

Preprint of Bio-Design and Manufacturing (unedited)

4 Experiments

4.1 Setup

We developed a DFCR prototype that integrates both drug delivery and tissue sampling functionalities (Fig. 6). The majority of the prototype's components, such as the shell, shaft, and ratchet, were constructed using regular photosensitive resin via stereolithography (SLA) 3D printing (SOGAWORKS, China). The dimensions of the notch reserved for biopsy were 5 × 5 mm^2. An elastic pawl, made of a black soft rubber material (TPU, 70A) using an FDM 3D printer (Bambu Lab, China), worked alongside the ratchet to ensure unidirectional rotation. The blade, constructed from red wax resin, included a sharp stainless-steel edge produced via electrical discharge machining. The

MTS comprised three N35 magnets and two bearings sourced from Alibaba Co. (China). The drug storage chamber contained approximately 0.3 mL of 10% semisolid PVA gel stained with blue food coloring (McCormicK, USA) to simulate a drug for treating stomach diseases. All the fixed internal parts and shells were bonded using a medical-grade adhesive (Loctite 435, Henkel Investment Co., Ltd., China). Once assembled, the final DFCR had a diameter of 12 mm and a length of 45 mm.

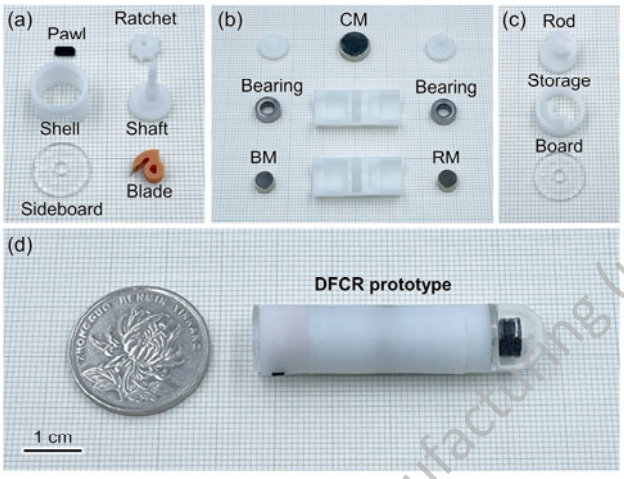

Figure 6 Photographs of the components of the DFCR and final product: (a) tissue biopsy module, (b) MTS module, (c) drug delivery module, and (d) assembled DFCR prototype.

Based on the two motion control modes (i.e., destination reaching and orientation adjusting), a five-degree-of-freedom PMD platform with an EPM end-effector was also developed to generate the required magnetic field for DFCR motion and function triggering (Fig. 7). The platform enabled rotational motion around the x- and z-axes through direct connections to the motor shaft and worm-gear transmission, respectively (Table 1). Translational motion along the x-and y-axes was achieved using synchronized pulleys to maintain a constant motor position during horizontal movement. Vertical translation was facilitated by a screw with high-loading and self-locking capabilities. The EPM provided a range of motion of $300 \times 300 \times 200$ mm^3, effectively covering the typical size range of an adult stomach [35]. The mechanisms were powered by stepper motors controlled by an STM32 (STMicroelectronics, Switzerland), and the human–machine interface (HMI) for command communication was programmed using LabVIEW (National Instruments, USA).

Preprint of Bio-Design and Manufacturing (unedited)

4.2 Force evaluation

To investigate the feasibility of drug delivery and lesion biopsy, the two output torques of the RM and BM were measured while applying a unidirectional magnetic field. Additionally, the anchoring force acting on the capsule was quantified during microsurgery to ensure the stability of the working process. The radially distributed magnetic field of the EPM was also examined to verify the effectiveness of the triggering mechanism. The obtained results were then compared with previous simulation data for further analysis.

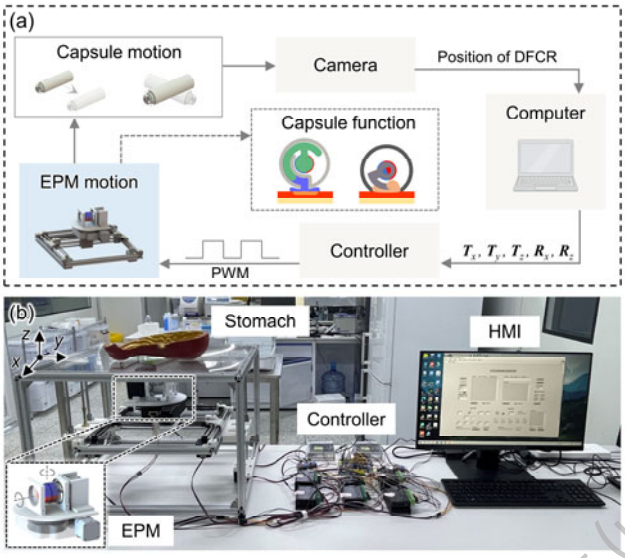

Figure 7 PMD system for capsule manipulation. (a) Block diagram of the approach for controlling the robotic capsule, where $\boldsymbol{T}_x, \boldsymbol{T}_y, \boldsymbol{T}_z, \boldsymbol{R}_x, \boldsymbol{R}_z$ represent the five-degree-of-freedom motion information of the EPM. (b) PMD system prototype. Abbreviations: PMD, permanent magnet driving; HMI, human–machine interface.

Table 1 Major parameters of the PMD system.

DOF	Type	Range	Accuracy
Rotation around x	Direct Connection	360 deg	0.1125 deg
Rotation around z	Worm gear	360 deg	0.005 deg
Translation along x	Synchronous pulley	300 mm	0.1 mm
Translation along y	Synchronous pulley	300 mm	0.1 mm
Translation along z	Lead- screw	200 mm	0.005 mm

Preprint of Bio-Design and Manufacturing (unedited)

Figure 8a and b illustrate the conceptual and experimental setup for measuring the two output torques. The EPM was positioned on a linear stand to facilitate vertical motion, while the DFCR was placed on a fixed stage within the effective range of the magnetic field generated by the EPM. Both the BM and RM inside the capsule were coaxially connected to rollers of the same diameter. By attaching an inextensible string between the roller and the load cell (Nscing Co., SH-III, China), the aimed torques were calculated as follows:

$$\boldsymbol{T}_m = \boldsymbol{F}_p \cdot R, \quad (12)$$

where $\boldsymbol{T}_m, \boldsymbol{F}_p, R$ are the working torque under the dual impact of the CM and EPM, the pulling force on the string, and the rotation radius of the roller, respectively. The EPM

was pre-adjusted to align with the magnetization direction of the CM. During the torque measurement process, the EPM moved toward the DFCR from a distance of 80 mm to 30 mm with a step interval of 1 mm to apply an enhancing unidirectional magnetic field. As the string only experiences tension forces, its orientation had to be adjusted based on the direction of $\boldsymbol{T}_m$.

When the BM and RM rotated by $\pi/2$, the output torque reached its maximum, initiating the functions of the drug-pushing rod and biopsy blade. Figure 8c and d show the measured drug-delivery and tissue-biopsy torques, which aligned closely with the simulated values. Minor discrepancies may have stemmed from assembly inaccuracies and friction among the internal components. The RM and BM generated specific torques when the EPM was positioned 62 mm and 43 mm away from the capsule, respectively. As this distance decreased to 44 mm, the RM's drug-delivery torque was 3.129 mNm, with a calculated drug-pushing force of 894 mN. At 34 mm, the BM's biopsy torque reached 6.860 mNm, and the corresponding biopsy stress was calculated at 22.87 MPa using Eq. (3). The experimental data confirmed that both the RM and BM are capable of generating sufficient torque for surgical procedures once their operational sequence is firmly established.

Figure 9a and b show the schematic and experimental setup for measuring the anchoring force. The EPM was placed on a vertical linear stand. To better replicate the gastrointestinal environment, a freshly isolated pig stomach was used to conduct the experiment. The DFCR was positioned on the stomach, with one end connected to a load cell (Nscing Co., SH-III) via a polymer string. The force gauge moved at a consistent speed in a linear act controlled by a stepper motor. The capsule was propelled at a uniform speed, and the anchoring force was subsequently determined using the following equations:

$$\begin{cases} \omega \boldsymbol{a} = \boldsymbol{F}_t - \boldsymbol{f} \\ \boldsymbol{F}_N = \boldsymbol{F}_A + \omega \boldsymbol{g} \\ \boldsymbol{f} = \mu_f \boldsymbol{F}_N \end{cases}, \quad (13)$$

where $\boldsymbol{a}$ represents capsule acceleration, with the DFCR moving at a constant speed resulting in $|\boldsymbol{a}| = 0$. In these equations, $\boldsymbol{F}_N, \boldsymbol{F}_A, \boldsymbol{F}_t, \boldsymbol{f}$ denote the normal force, anchoring force, tensile force, and friction force, respectively. Initially, the friction coefficient μ_f was measured in the absence of the EPM. Subsequently, the EPM was adjusted in 1-mm increments to approach the capsule and record the tensile force at each step. Additionally, a teslameter (Tunkia Co., TD8620, China) was utilized to measure the magnetic field strength every 1 mm along the radial direction of the EPM.

Preprint of Bio-Design and Manufacturing (under review)

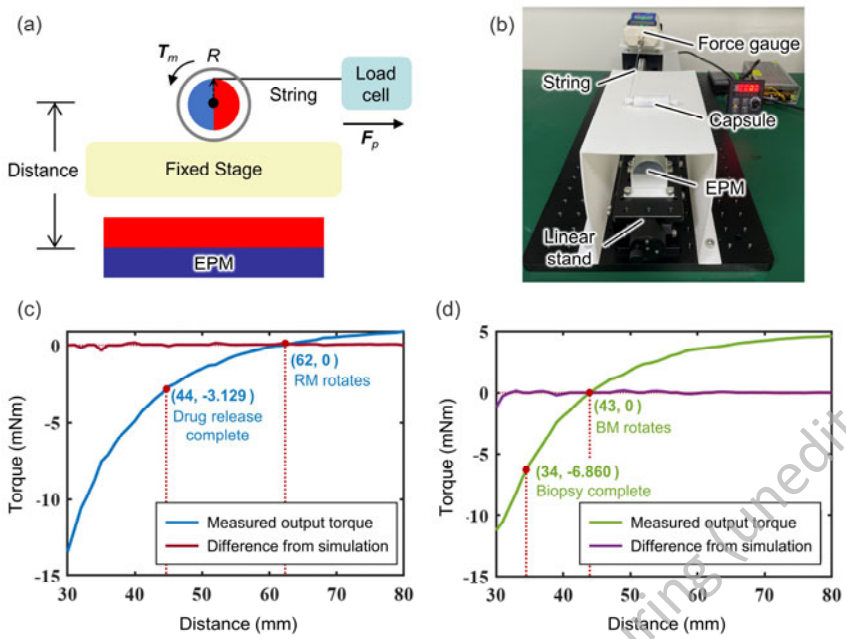

Figure 8 Measurements of the output torque. (a) Conceptual diagram for assessing the output torque. (b) Experimental platform. (c) Drug release torque corresponds to distances between the EPM and MTS. (d) Tissue biopsy torque as the EPM approaches.

Based on the analysis of the anchoring force, whose results are presented in Figure 9c and 9d, the experimental data closely aligned with the simulated values. Minor discrepancies may be attributed to inaccuracies in the magnetic field, potentially arising from an angular misalignment between the teslameter probe and the direction of the external magnetic field as well as from variations in the anchoring force due to irregular folds on the stomach surface that disrupted the linear motion of the capsule. As the distance between the EPM and the DFCR decreased from 80 mm to 61 mm, the anchoring force gradually increased. Only the CM was attracted, while the other two magnets were repelled. When the distance was 62 mm and the magnetic field strength reached 17.32 mT, the RM began to rotate and the anchoring force increased to 0.194 N. The curve's growth rate accelerated from 61 mm to 44 mm due to the absence of repulsion from the RM. The drug was released at 44 mm under an external magnetic field of 67.59 mT. At 43 mm, with a magnetic field of 72.55 mT, the BM aligned its magnetic moment with the external field, resulting in an anchoring force of 0.974 N. The trend further intensified from 45 mm to 33 mm due to the magnet's attractive force. Tissue was collected via biopsy at 34 mm under a magnetic field of 151.82 mT. Throughout the procedure, the DFCR remained stably anchored to the lesion area, confirming the system's stability.

Preprint of BIO-Design and Manufacturing (unedited)

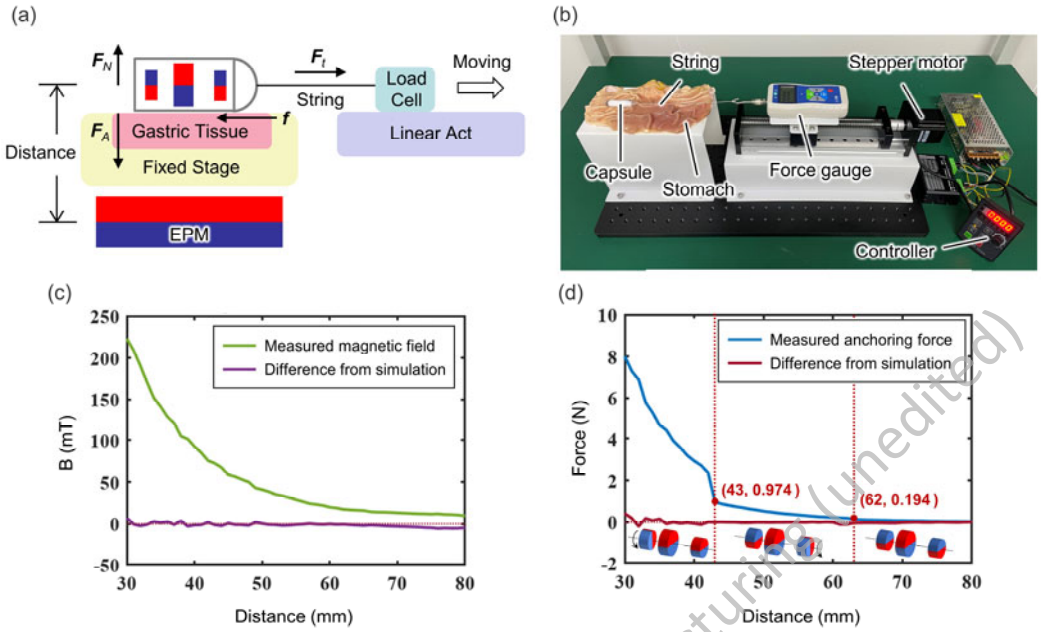

Figure 9 Measurement of the anchoring force: (a) schematic diagram for estimating the anchoring force, (b) experimental setup, (c) magnetic field distribution results as the EPM approaches, (d) anchoring force value of the DFCR.

Preprint of Bio-Design and Manufacturing (unedited)

4.3 Motion validation

To evaluate the effectiveness of the motion model, the DFCR was tested on an ex vivo porcine stomach. The stomach's surface folds were uniformly simplified into uphill and downhill slopes. The required magnetic field strength to propel the capsule forward or adjust its orientation increased in the presence of protruding tissues and decreased in the presence of concave tissues. Throughout the motion, the magnetic field strength varied from 14.01 mT to 16.25 mT. Prior to the experiment, the stomach tissue was moistened with water to simulate a patient drinking water and swallowing the capsule.

Figure 10 and Video S1 depict the motion of the DFCR. The green dot indicates the starting point of the capsule, while the red dot marks the target lesion. Initially, the capsule moved uniformly in the *y* direction while rotating around its cylindrical axis and the *z*-direction, which caused it to roll rightward and rotate clockwise. A pre-positioning method using a front-mounted camera was employed to observe the stomach and identify lesions. As the EPM moved past the capsule along the y-axis, the force exerted by the external gradient magnetic field on the capsule overcame the torque produced by the rotating magnetic field, causing the capsule to slide toward the target area. Eventually, the capsule aligned directly above the EPM, where the rotational torque became the dominant force, propelling the capsule to its destination. Throughout this process, the uneven distribution of the magnetic field around the EPM and the interference torque from the gastric surface folds resulted in the DFCR moving slightly backward.

The motion test confirmed the reliability of the wireless DFCR control. By appropriately adopting the destination-reaching and orientation-adjusting methods, the capsule safely and accurately reached its target location. Additionally, the intensity of the driving

magnetic field remained below the triggering threshold of the MTS, thus premature triggering of drug release and tissue biopsy functions was not observed during the movement.

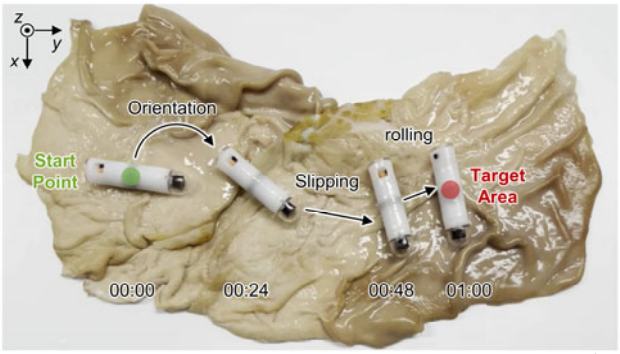

Figure 10 Image illustrating the motion of the DFCR through the porcine stomach, including its position and orientation at certain specific moments.

4.4 In vitro test

The experimental procedure for drug release is depicted in Fig. 11a and Video S2. Initially, the capsule was guided to the target site, where its outlet was aligned with the designated area. Upon application of an external magnetic field to the RM, the rod began to rotate counterclockwise by $\pi/2$, enabling drug delivery through the outlet to the target location. As the external magnetic field decreased, the rod returned to its original position, allowing for repeated drug administration by cyclically strengthening and weakening the magnetic field, thereby optimizing drug release. Ultimately, upon relocating the capsule, the release of the blue-colored drug at the target site became observable. Throughout this entire process, the biopsy module remained stationary.

In the case of tissue biopsy (Fig. 11b), a section of an ex vivo pig stomach was partially cut to create a small adhered protrusion that simulated hyperplastic tissue. As observed for the drug delivery operation, the DFCR was initially guided to the target area, allowing the hyperplastic tissue to enter the capsule through the notch. As the activated magnetic field was applied, the blade was propelled by the BM to rotate and scrape the tissue inside. The removal of the magnetic field locked the blade in place due to the ratchet and pawl mechanism, effectively sealing the collected tissue within the capsule.

According to the experimental results (Fig. 11c-d), the designed functional modules were capable of releasing the stored drug almost completely (0.3 mL, basically no residue in the chamber) and successfully extracting approximately 1.8 mm^3 of tissue (1.8 mm × 1 mm × 1 mm) from the target location, thereby satisfying the fundamental requirements for medical diagnosis and treatment. To ensure the reliability and consistency of the experimental data, five tests were conducted for both the drug delivery and biopsy functions. The drug delivery was 100% successful, meaning that the drug was completely released to the target location. The biopsy sampling had a success rate of 80%, with an average volume of sampled tissue of approximately 1.526 mm^3. Additionally, these samples were subjected to histological analysis. First, each sample was placed in phosphate-buffered saline (PBS) and homogenized using ultrasonic treatment. It was

Preprint of Bio-Design and Manufacturing (unedited)

then suspended in PBS and stained with 4', 6-diamidino-2phenylindole solution. In a dark environment, the tissue precipitate was collected and resuspended in PBS, and a portion of the suspension was placed on a slide for observation under a fluorescence microscope. In the fluorescence microscopy image of a sampled tissue shown in Fig. 11d, the blue regions represent fresh animal cells, further validating the effectiveness of the biopsy function.

Notably, to simplify targeted drug delivery and biopsy, this experiment employed an open-outlet design, including a drug outlet and a notch. The drug storage chamber was filled with a semisolid formulation to reduce the risk of accidental release at non-target sites. In comparison to liquid formulations, semisolid drugs, which exhibit higher viscosity and concentration, can demonstrate their functions more effectively. In potential clinical applications, degradable films (as coatings) or soluble ice materials can be positioned at the capsule's openings to seal the chamber, thereby preventing premature drug release or damage as well as the inadvertent entry of foreign substances. Specific degradation triggers, such as temperature, pH, or enzymes, can be identified based on the physiological or pathological conditions present in different regions of the gastrointestinal tract [36].

Preprint of Bio-Design and Manufacturing (Unedited)

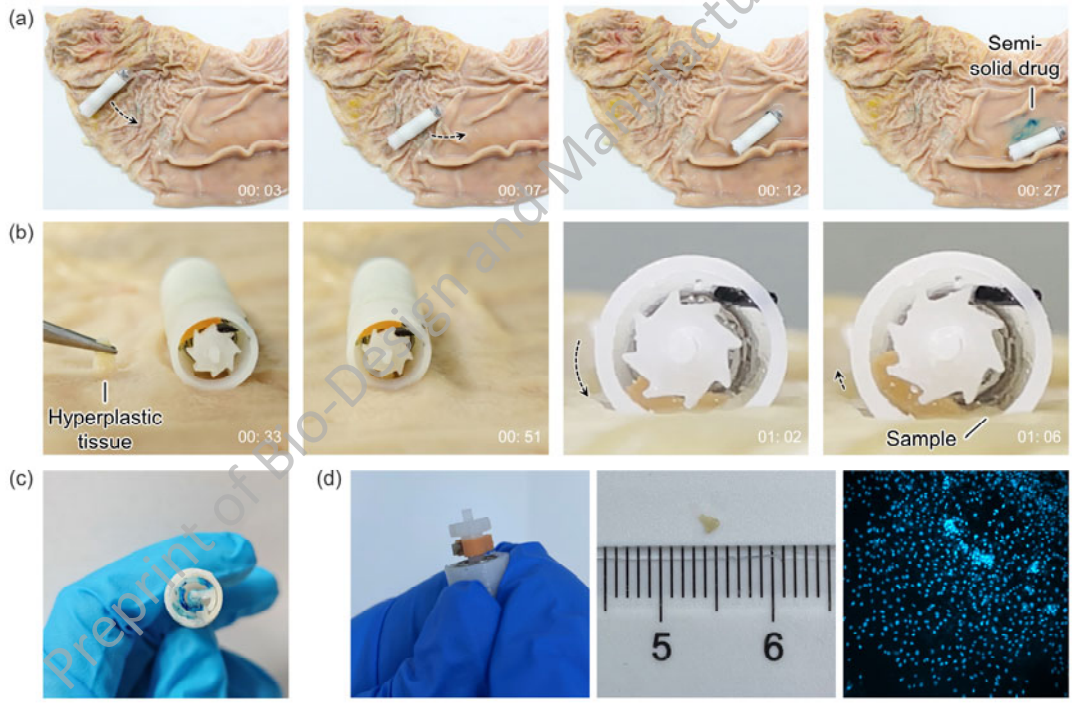

Figure 11 Workflow of the procedure and experimental results: (a) drug release experiment, (b) tissue biopsy experiment, (c) drug delivery module after the experiments, (d) sampled tissue and its fluorescence microscopy image.

5 Discussion and outlook

In this study, we introduced a DFCR activated by a MTS. The innovative MTS system, consisting of three magnets integrated within the capsule, was shown to enable both sequential medication delivery and lesion biopsies within a controlled, unidirectional

magnetic field. A permanent magnet drive platform with five degrees of freedom has been developed to facilitate the wireless control of the DFCR. Torque measurements indicated that the capsule robot generated 894 mN of thrust for medication delivery and 22.87 MPa of stress for sampling when exposed to external magnetic fields of 67.59 mT and 151.82 mT, respectively. Motion experiments confirmed the capsule's capability to adjust its position, detect lesions, and navigate to specific targets. Furthermore, ex vivo trials on porcine stomachs demonstrated the successful delivery of 0.3 mL of medication and retrieval of 1.8 mm^3 samples.

Unlike conventional capsule robots that are limited to a single function, the newly developed DFCR can perform multiple diagnostic and therapeutic tasks within a confined space, thereby expanding the clinical possibilities of capsule endoscopy for surgical tasks. Recent studies have proposed enhancing capsule functionality through modular designs, where multiple independent robots collaborate to perform specialized tasks in restricted environments [37-40]. However, challenges such as the reliability of docking mechanisms, suitability for larger spaces like the stomach, and the risks of retention in intestinal bends need to be addressed. These limitations indicate that the research is still in its early stages, and the practical implementation of multiple integrated functions has not yet been achieved. In contrast, our proposed MTS provides a promising alternative by addressing the integration problem to a significant extent and offering the advantage of cost-effectiveness for practical implementation [41].

Currently, this novel DFCR and its control platform require further development. For instance, we have only demonstrated the independence of the two functions in the specific application scenario of administering medication before biopsy. Although it is feasible to redesign the sequence of these functions based on the MTS and utilize them independently, in practice, the diagnostic and therapeutic functions are not fully independent. Additionally, with regard to the clinical translation of the DFCR, potential side effects and risks must be considered. The newly developed capsule robot is approximately 1.5 times longer than the currently used commercial capsule endoscopes (typically 25–30 mm), which means it is more difficult for patients to swallow and also significantly increases the risk of complications such as intestinal obstruction. Optimizing the axial dimension of the MTS and employing a soft polymer shell along with flexible magnets, instead of the current hard shell and rigid magnets, could enhance patency in narrow environments like the intestines. Considering the requirements of biocompatibility, future capsule prototypes should be constructed using medical-grade plastics, such as polyvinyl chloride and polyethylene, due to their lightweight nature and appropriate stiffness. Biocompatibility tests are also essential to prevent infections in gastrointestinal tissues. Furthermore, an array of magnetic sensors can be arranged around the PMD platform to provide physicians with real-time information on the capsule's location, improve the accuracy of the capsule's movements through closed-loop feedback, and prevent accidental drug release or biopsy by monitoring the distance between the EPM and the magnets inside the capsule.

In addition to solving the above challenges, future work should explore additional functional applications of the capsule robot and conduct in vivo testing to fully harness the DFCR's potential in clinical surgery. We believe that WCE robots will eventually replace traditional wired endoscopes, bringing the concept of a "capsule surgeon" to fruition [42].

Journal of Bio-Design and Manufacturing (Unedited)

Acknowledgements This work was supported by the National Natural Science Foundation of China (No. 52105072), Zhejiang Provincial Natural Science Foundation of China under No. LZ24E050004, Jiangsu Provincial Outstanding Youth Program (No. BK20230072), a grant from Suzhou Industrial Foresight and Key Core Technology Project (No. SYC2022044), and grants from Jiangsu QingLan Project and Jiangsu 333 high-level talents.

Author contributions QC was involved in conceptualization and writing the original draft. YP helped in the investigation and writing. YQHZ and YNJ conducted a deep review and editing. GFG and HYY gave some advice. FZN and DH helped revise the paper, supervised the work, and applied for funds. All authors have read and approved this manuscript for publication.

Declarations

Conflict of interest

HYY is an editor-in-chief for *Bio-Design and Manufacturing* and was not involved in the editorial review or the decision to publish this article. The authors declare that they have no conflict of interest.

Ethical approval

This study does not contain any studies with human or animal subjects performed by any of the authors.

References

1. Poorolajal J, Moradi L, Mohammadi Y, Cheraghi Z, Gohari-Ensaf F (2020) Risk factors for stomach cancer: a systematic review and meta-analysis. Epidemiol Health 42:e2020004. https://doi.org/10.4178/epih.e2020004

2. Thrift AP, Wenker TN, El-Serag HB (2023) Global burden of gastric cancer: epidemiological trends, risk factors, screening and prevention. Nat Rev Clin Oncol 20(5):338-349. https://doi.org/10.1038/s41571-023-00747-0

3. Ferlay J, Colombet M, Soerjomataram I, Parkin DM, Pineros M, Znaor A, Bray F (2021) Cancer statistics for the year 2020: An overview. Int J Cancer. https://doi.org/10.1002/ijc.33588

4. Boskoski I, Costamagna G (2019) Endoscopy robotics: Current and future applications. Dig Endosc 31(2):119-124. https://doi.org/10.1111/den.13270

5. Rogalski P, Daniluk J, Baniukiewicz A, Wroblewski E, Dabrowski A (2015) Endoscopic management of gastrointestinal perforations, leaks and fistulas. World J Gastroenterol 21(37):10542-10552. https://doi.org/10.3748/wjg.v21.i37.10542

Preprint of Bio-Design and Manufacturing (unedited)

6. Pardo E, Camus M, Verdonk F (2022) Anesthesia for digestive tract endoscopy. Curr Opin Anaesthesiol 35(4):528-535. https://doi.org/10.1097/ACO.0000000000001162

7. Geropoulos G, Aquilina J, Kakos C, Anestiadou E, Giannis D (2021) Magnetically Controlled Capsule Endoscopy Versus Conventional Gastroscopy: A Systematic Review and Meta-Analysis. J Clin Gastroenterol 55(7):577-585. https://doi.org/10.1097/MCG.0000000000001540

8. Iddan G, Meron G, Glukhovsky A, Swain P (2000) Wireless capsule endoscopy. Nature 405(6785):417-417. https://doi.org/10.1038/35013140

9. Luo Y-Y, Pan J, Chen Y-Z, Jiang X, Zou W-B, Qian Y-Y, Zhou W, Liu X, Li Z-S, Liao Z (2019) Magnetic Steering of Capsule Endoscopy Improves Small Bowel Capsule Endoscopy Completion Rate. Dig Dis Sci 64(7):1908-1915. https://doi.org/10.1007/s10620-019-5479-z

10. Son D, Dogan MD, Sitti M (2017) Magnetically actuated soft capsule endoscope for fine-needle aspiration biopsy. In: 2017 IEEE International Conference on Robotics and Automation (ICRA). pp 1132-1139. https://doi.org/10.1109/ICRA.2017.7989135

11. Wilding I, Hirst P, Connor A (2000) Development of a new engineering-based capsule for human drug absorption studies. Pharm Sci Technol Today 3(11):385-392. https://doi.org/https://doi.org/10.1016/S1461-5347(00)00311-4

12. Zu S, Zhang Z, Liu Q, Wang Z, Song Z, Guo Y, Xin Y, Zhang S (2022) 4D printing of core–shell hydrogel capsules for smart controlled drug release. Bio-Des Manuf 5(2):294-304. https://doi.org/10.1007/s42242-021-00175-y

13. Yu W, Rahimi R, Ochoa M, Pinal R, Ziaie B (2015) A Smart Capsule With GI-Tract-Location-Specific Payload Release. IEEE Trans Biomed Eng 62(9):2289-2295. https://doi.org/10.1109/TBME.2015.2418340

14. Chen W-W, Yan G-Z, Liu H, Jiang P-P, Wang Z-W (2014) Design of micro biopsy device for wireless autonomous endoscope. Int J Precis Eng Manuf 15(11):2317-2325. https://doi.org/10.1007/s12541-014-0596-2

15. Pan X, Ma T, Li P, Jiang X, Song S, Meng MQH (2018) A novel intestinal microcapsule endoscope robot with biopsy function. In: 2018 IEEE International Conference on Cyborg and Bionic Systems (CBS). pp 308-312. https://doi.org/10.1109/CBS.2018.8612210

16. Rehan M, Al-Bahadly I, Thomas DG, Avci E (2020) Capsule robot for gut microbiota sampling using shape memory alloy spring. Int J Med Robot Comput Assist Surg 16(5):e2140. https://doi.org/https://doi.org/10.1002/rcs.2140

17. Son D, Gilbert H, Sitti M (2019) Magnetically Actuated Soft Capsule Endoscope for Fine-Needle Biopsy. Soft Robot 7(1):10-21. https://doi.org/10.1089/soro.2018.0171

18. Lee J, Sohn SW, Lee H, Park S (2022) Open-close Mechanism of Magnetically Actuated Capsule for Multiple Hemostatic Microneedle Patch Delivery. Int J Control Autom Syst 20(7):2285-2296. https://doi.org/10.1007/s12555-021-0306-7

Preprint of Bio-Design and Manufacturing (unedited)

19. Guo S, Zhang L, Yang Q (2019) The Structural Design of a Magnetic Driven Wireless Capsule Robot for Drug Delivery. In: 2019 IEEE International Conference on Mechatronics and Automation (ICMA). pp 844-849. https://doi.org/10.1109/ICMA.2019.8816504

20. Hoang MC, Le VH, Kim J, Choi E, Kang B, Park JO, Kim CS (2019) Untethered Robotic Motion and Rotating Blade Mechanism for Actively Locomotive Biopsy Capsule Endoscope. IEEE Access 7:93364-93374. https://doi.org/10.1109/ACCESS.2019.2927894

21. Leon-Rodriguez H, Park SH, Park JO (2020) Testing and Evaluation of Foldable Biopsy Tools for Active Capsule Endoscope. In: 2020 20th International Conference on Control, Automation and Systems (ICCAS). pp 473-479. https://doi.org/10.23919/ICCAS50221.2020.9268232

22. Liu L, Towfighian S, Hila A (2015) A Review of Locomotion Systems for Capsule Endoscopy. IEEE Rev Biomed Eng 8:138-151. https://doi.org/10.1109/RBME.2015.2451031

23. Xu X, Huo Z, Guo J, Liu H, Qi X, Wu Z (2020) Micromotor-derived composites for biomedicine delivery and other related purposes. Bio-Des Manuf 3(2):133-147. https://doi.org/10.1007/s42242-020-00072-w

24. Ye D, Zhang F, Yuan S, Song S, Meng MQH (2019) Magnetically Driven Wireless Capsule Robot with Targeting Biopsy Function. In: 2019 IEEE International Conference on Robotics and Biomimetics (ROBIO). pp 1222-1227. https://doi.org/10.1109/ROBIO49542.2019.8961521

25. Simi M, Gerboni G, Menciassi A, Valdastri P (2013) Magnetic Torsion Spring Mechanism for a Wireless Biopsy Capsule. J Med Devices 7(4). https://doi.org/10.1115/1.4025185

26. Zhou H, Alici G (2019) A Novel Magnetic Anchoring System for Wireless Capsule Endoscopes Operating Within the Gastrointestinal Tract. IEEE-ASME Trans Mechatron 24(3):1106-1116. https://doi.org/10.1109/TMECH.2019.2909288

27. Alici G (2015) Towards soft robotic devices for site-specific drug delivery. Expert Rev Med Devices 12(6):703-715. https://doi.org/10.1586/17434440.2015.1091722

28. Woods SP, Constandinou TG (2016) A compact targeted drug delivery mechanism for a next generation wireless capsule endoscope. J Microbio Robot 11(1):19-34. https://doi.org/10.1007/s12213-016-0088-9

29. Hopper AD, Cross SS, Sanders DS (2008) Patchy villous atrophy in adult patients with suspected gluten-sensitive enteropathy: is a multiple duodenal biopsy strategy appropriate? Endoscopy 40(03):219-224. https://doi.org/10.1055/s-2007-995361

30. Catassi C, Fasano A (2010) Celiac disease diagnosis: simple rules are better than complicated algorithms. Am J Med 123(8):691-693. https://doi.org/10.1016/j.amjmed.2010.02.019

Preprint of Bio-Design and Manufacturing (unedited)

31. Lucarini G, Ciuti G, Mura M, Rizzo R, Menciassi A (2015) A New Concept for Magnetic Capsule Colonoscopy Based on an Electromagnetic System. Int J Adv Robot Syst 12(3). https://doi.org/10.5772/60134

32. Yang Z, Zhang L (2020) Magnetic Actuation Systems for Miniature Robots: A Review. Adv Intell Syst 2(9). https://doi.org/10.1002/aisy.202000082

33. Kummer MP, Abbott JJ, Kratochvil BE, Borer R, Sengul A, Nelson BJ (2010) OctoMag: An Electromagnetic System for 5-DOF Wireless Micromanipulation. IEEE Trans Robot 26(6):1006-1017. https://doi.org/10.1109/tro.2010.2073030

34. Lee C (2016) Feasibility study of electromagnetic guidance system for intestinal capsule endoscope. In: 2016 IEEE International Conference on Robotics and Biomimetics (ROBIO). pp 1542-1547. https://doi.org/10.1109/ROBIO.2016.7866546

35. Lamart S, Imran R, Simon SL, Doi K, Morton LM, Curtis RE, Lee C, Drozdovitch V, Maass-Moreno R, Chen CC, Whatley M, Miller DL, Pacak K, Lee C (2013) Prediction of the location and size of the stomach using patient characteristics for retrospective radiation dose estimation following radiotherapy. Phys Med Biol 58(24):8739-8753. https://doi.org/10.1088/0031-9155/58/24/8739

36. Chu JN, Traverso G (2022) Foundations of gastrointestinal-based drug delivery and future developments. Nat Rev Gastroenterol Hepatol 19(4):219-238. https://doi.org/10.1038/s41575-021-00539-w

37. Guo S, Yang Q, Bai L, Zhao Y (2018) Development of Multiple Capsule Robots in Pipe. Micromachines 9(6):259. https://doi.org/10.3390/mi9060259

38. Zheng L, Guo S, Wang Z, Tamiya T (2021) A Multi-Functional Module-Based Capsule Robot. IEEE Sens J 21(10):12057-12067. https://doi.org/10.1109/JSEN.2021.3058354

39. Peker F, Ferhanoğlu O (2021) Multi-Capsule Endoscopy: An initial study on modeling and phantom experimentation of a magnetic capsule train. J Med Biol Eng 41(3):315-321. https://doi.org/10.1007/s40846-021-00610-6

40. Peker F, Ferhanoğlu O (2024) Active distance control in multi-capsule endoscopy via closed loop electromagnetic force between capsules. Med Biol Eng Comput 62(4):1153-1163. https://doi.org/10.1007/s11517-023-02997-7

41. Mundaca-Uribe R, Askarinam N, Fang RH, Zhang L, Wang J (2023) Towards multifunctional robotic pills. Nat Biomed Eng. https://doi.org/10.1038/s41551-023-01090-6

42. Cao Q, Deng R, Pan Y, Liu R, Chen Y, Gong G, Zou J, Yang H, Han D (2024) Robotic wireless capsule endoscopy: recent advances and upcoming technologies. Nat Commun 15(1):4597. https://doi.org/10.1038/s41467-024-49019-0

Preprint of Bio-Design and Manufacturing (unedited)